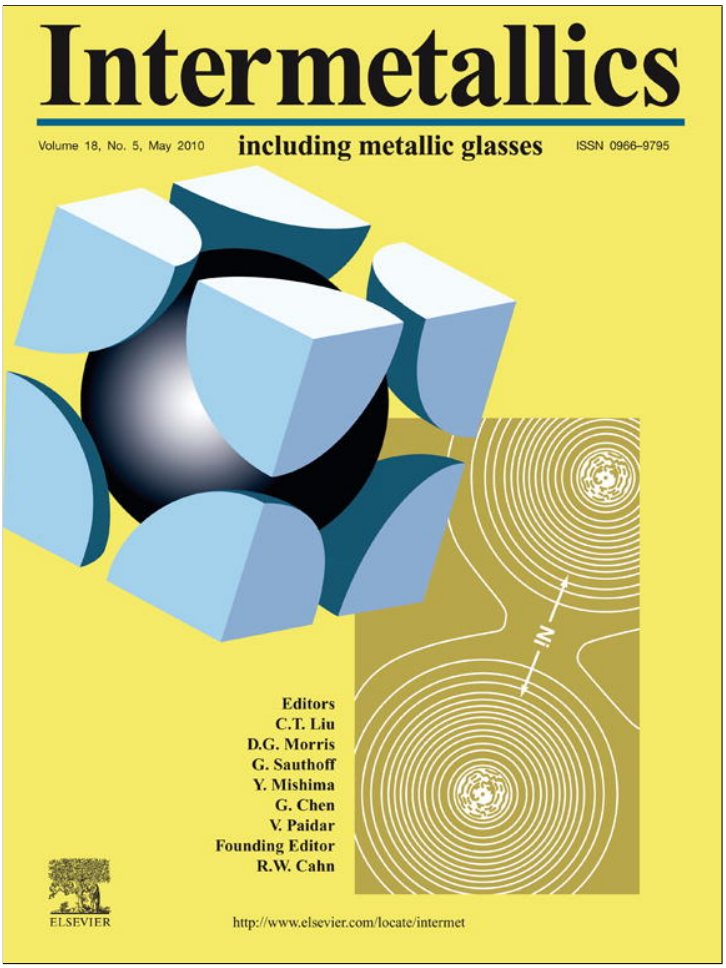

Intermetallics 18 (2010) 945–953

Contents lists available at ScienceDirect

Intermetallics

journal homepage: www.elsevier.com/locate/intermet

Thermal and physical properties of B2 Al–Ir–X (X = Ni, Ru, Pd, Co, Fe) alloys

M.F. del Grosso [a,b,c], H.O. Mosca [a,d], G. Bozzolo [e,*]

[a] Gerencia de Investigación y Aplicaciones, Comisión Nacional de Energía Atómica, Av. Gral. Paz 1499 (B1650KNA), San Martín, Argentina
[b] GCMN, UTN, FRG Pacheco, Av. Hipólito Yrigoyen 288, Gral. Pacheco, Argentina
[c] CONICET, Argentina
[d] Instituto Sabato, Universidad Nacional de San Martín/CNEA, Av. Gral. Paz 1499 (B1650KNA), San Martín, Argentina
[e] Physics Department, Loyola University Maryland, 4501 N. Charles St., Baltimore, MD 21210, USA

ARTICLE INFO

Article history:
Received 17 November 2009
Received in revised form
22 December 2009
Accepted 14 January 2010
Available online 26 February 2010

Keywords:
A. Ternary alloy systems
B. Thermal properties
E. Simulations, atomistic
E. Physical properties, miscellaneous

ABSTRACT

The thermal and physical properties of B2 Al–Ir–X (X = Ni, Ru, Pd, Co, Fe) alloys are presented for the whole B2 field of each ternary system. Using the BFS method for alloys, the phase structure, long and short range ordering behavior and the site preference trends for X additions to AlIr are discussed, and results are shown for the cohesive energy, equilibrium lattice parameter, bulk modulus, coefficient of thermal expansion, heat capacity, and melting temperature for the five ternary systems in the B2 field.

1. Introduction

Motivated by a growing number of specific applications, experimental work on alloying additions to B2 AlIr has increased significantly. Interest in this system arises from the need for new oxidation resistance coatings for use in high temperature structural materials due to the high melting point of Ir and the oxidation properties of AlIr. Iridium exhibits much lower oxygen permeability than SiO_2 and Al_2O_3 [1], making it a good candidate for oxygen diffusion barriers. However, Ir itself forms Ir oxides [2], so alloying with Al has been investigated as a way to inhibit or altogether suppress oxidation by forming an Al_2O_3 layer [3]. In order to improve their mechanical and thermal properties and oxidation behavior, ternary Ni, Co, or Fe additions [4] have been extensively studied. These elements have the potential of stabilizing the B2 AlIr phase (all three elements form stable B2 aluminides), improve the oxidation resistance, and reduce costs. Promising results were found for moderate amounts of Ni and Co but not for Fe. Co, however, exhibited dramatic improvements in oxidation resistance [5].

Concern on the role of ternary Al–Ir–X systems is not limited to additions to B2 AlIr, as the fundamental properties mentioned above extend to the case of superalloys. Parallel studies were recently carried out to examine Ir-based superalloys, driven by the high melting point of Ir. Such alloys also have higher strength than B2 NiAl and pure Ir with the fcc structure, and form aluminium oxide on the surface, resulting in good oxidation resistance [3,4]. The effectiveness of Ni as a solid-solution hardening element in fcc Ir and the mutual solubility of Ir and Ni allow for suitable control of the microstructure and mechanical properties. For these reasons, recent experimental work has concentrated on the details of the Ir–Ni–Al ternary system [6,7] and the formation of B2 AlIr precipitates in the fcc matrix, as well as the density reduction effect from substituting Ni for Ir [7]. More recent studies on the phase equilibria in Ir–Ni–Al were performed to further the understanding of the diffusion process between AlIr and Ni-base superalloys [8].

There is yet one more instance where knowledge of the characteristics of ternary Al–Ir–X systems is of technological relevance. Concentrating on AlRu alloys, the inherent brittleness usually associated with intermetallic bonding, sparked interest on B2 AlIr-based alloys as such problem can be countered with the presence of a second phase triggered by the addition of small amounts of an element that improves ductility [9–13]. The Al–Ir system was selected for further study [9] due to its high temperature strength and reasonable toughness at room temperature [10]. The fact that superior strength and oxidation resistance is bound to be found in the Ar–Ir–Ru system and the very limited data available for this system, motivated studies to identify the resulting narrow continuous Al-(Ir,Ru) B2 field in the ternary Al–Ir–Ru phase diagram [11].

* Corresponding author. Tel.: +1 410 995 4063.
E-mail address: guille_bozzolo@yahoo.com (G. Bozzolo).

0966-9795/$ – see front matter © 2010 Elsevier Ltd. All rights reserved.
doi:10.1016/j.intermet.2010.01.013

Table 1
LAPW-derived single element parameters for Al, Ir, Ni, Ru, Pd, Co, and Fe: lattice parameter (in Å), cohesive energy (in eV) and bulk modulus (in GPa).

	Lattice parameter (Å)	Cohesive energy (eV)	Bulk modulus (GPa)	p	α (Å^{-1})	l (Å)	λ (Å)
Al	3.2399	3.4226	69.54	4	1.76092	0.36229	1.01803
Ir	3.1128	8.1205	305.33	10	4.45742	0.27170	0.76348
Ni	2.7985	5.6001	198.75	6	3.05968	0.29494	0.82878
Ru	3.0484	6.5514	295.11	8	3.59741	0.25084	0.70486
Pd	3.1358	4.0148	172.86	8	3.48602	0.25297	0.71081
Co	2.7591	5.2842	250.90	6	3.03167	0.25681	0.72163
Fe	2.7565	4.7421	278.26	6	2.98305	0.23112	0.76348

The derivative parameters for solving the BFS equations, the principal quantum number, p; the average electron density, α; the scaling length of the zero-temperature universal binding energy relationship [21], l; and the screening length, λ, are also listed. See Ref. [19] for a description of these parameters and their role in the BFS equations.

These studies have been recently extended to consider quaternary Al–Ni–Ru–M systems (with M = Ir, among others) [13–15]. In line with all the aforementioned studies, some work has been done on the Al–Ir–Pd and Al–Ir–Os ternary systems to investigate alternative options for improving the melting point of Ir-based materials, as well as a more complete understanding of ternary additions of the platinum metals group [16,17].

This summary of the broad range of applications of AlIr-based materials and, in particular, B2-based compounds, suggests that a comprehensive survey of its physical and thermal properties for a number of ternary alloying additions, namely Ni, Ru, Pd, Co, and Fe, could be helpful in developing new compositions with specific properties for their various applications. To this effect, in this work we present results of an atomistic modeling study aimed to provide a detailed description of the thermal and physical properties for the whole range of concentrations where the B2 phase exists for Al–Ir–X (X = Ni, Ru, Pd, Co, Fe) alloys. This analysis is performed using the quantum approximate method of Bozzolo–Ferrante–Smith (BFS) [18] for the determination of the energetics of such alloys and its extension to finite temperature [19] for the calculation of thermal properties.

2. The BFS method for alloys

The BFS method for alloys [18] provides a straightforward procedure for the calculation of the energy of formation ΔH (the difference between the energy of the alloy and the sum of its individual components) of an arbitrary multicomponent alloy. As such, ΔH can written as the superposition of individual contributions ε_i from every atom in the alloy,

$$\Delta H = \sum_i \varepsilon_i = \sum_i (E_i' - E_i) \quad (1)$$

where E_i' and E_i represent the energy of atom i in the alloy and in an equilibrium pure crystal of species i, respectively. Each individual contribution ε_i is the sum of two components: a strain energy, ε_i^S, which strictly describes structural effects, and a chemical energy, ε_i^C, concentrating on the interaction between atoms of different species. The two terms are linked by a coupling function, g_i, which ensures the correct asymptotic behavior of the chemical energy term.

The strain energy contribution, ε_i^S, is computed as if each neighboring atom of the reference atom i is of the same species, but retaining the correct geometrical distribution in the alloy. Its calculation involves three basic parameters identifying each participating element i (cohesive energy, equilibrium lattice parameter, bulk modulus) [18]. Conversely, the chemical energy contribution, ε_i^C, is computed with every neighboring atom in equilibrium sites of a crystal of species i, retaining their chemical identity. In addition to the parameters used in the calculation of the strain energy term, the calculation of the chemical energy requires two perturbative parameters per pair of atomic species [18].

Table 2
LAPW-derived perturbative BFS parameters Δ_{AB} and Δ_{BA} for all the binary combinations used in this work.

A	B	Δ_{AB}	Δ_{BA}
Al	Ir	−0.051243	−0.037889
Al	Ni	0.039742	−0.040894
Al	Ru	−0.024831	−0.041861
Al	Pd	0.043055	−0.044204
Al	Co	0.051118	−0.041359
Al	Fe	0.117771	−0.041801
Ir	Ni	0.260878	−0.059048
Ir	Ru	0.098965	−0.049500
Ir	Pd	−0.034661	0.089209
Ir	Co	−0.052624	0.062156
Ir	Fe	−0.041710	0.055789

The single element parameters (cohesive energy, equilibrium lattice parameter, bulk modulus) and the BFS perturbative parameters for the different elements considered in this work (Al, Ir, Ru, Ni, Pd, Co, Fe) are listed in Tables 1 and 2, respectively. The single element parameters are obtained from the universal binding energy relationship of Rose et al. [20], computed from ab initio calculations using the linearized augmented plane wave method (LAPW) [21] for the total energy as a function of volume of each element. Additional LAPW calculations for the (generally metastable) B2 phases of every pair combination of them were performed for the determination of the BFS perturbative parameters, listed in Table 2. Validation of these parameters has been performed for some of them in previous BFS applications to related systems. These include the analysis of the ternary Al–Ni–Ru system [22], and the effect of ternary alloying additions to NiTi shape memory alloys [23]. In addition, some validation of the predicted results arises from the comparison of the experimental lattice parameter of specific ternary alloys. For $Al_{49}Ir_{51}$, Hosoda et al. [4] predict $a = 2.988$ Å, just below the calculated value in this work (<2%). Similar minor deviations are found for $Al_{51}Ir_{49}$ ($a = 2.981$ Å), and the ternary $Al_{51}Ir_{39}X_{10}$ (X = Ni, Co, Fe) alloys ($a = 2.972$, 2.969, and 2.969 Å, respectively).

3. Results and discussion

The properties of the different ternary alloys described in this work were obtained from the results of large scale atomistic simulations where the computational cells were treated to a decreasing temperature cycle leading to the most stable configuration at low temperature. Two types of simulations were performed. In the first case, the simulations were based on the traditional Monte Carlo–Metropolis algorithm (heretofore dubbed MCAS), which gives information on the ideal ground state of the system, and in the second case using a modified version of such algorithm meant to provide a more realistic evolution of the computational cell in terms of comparison with experiment (dubbed BANN). Details of these two types of simulations and their characteristics can be found in Ref. [18]. In both cases, it should be noted that the computational cell is restricted to retain its bcc uniform structure, as all the chosen concentrations belong to the respective B2 field of each ternary system. MCAS simulations, which are meant to provide information on the ideal ground state, are thus limited in terms of interpreting the phase structure that results. At most, they indicate the temperatures at which the formation of a second phase starts (if it exists) and its composition, but nothing can be said with certainty in terms

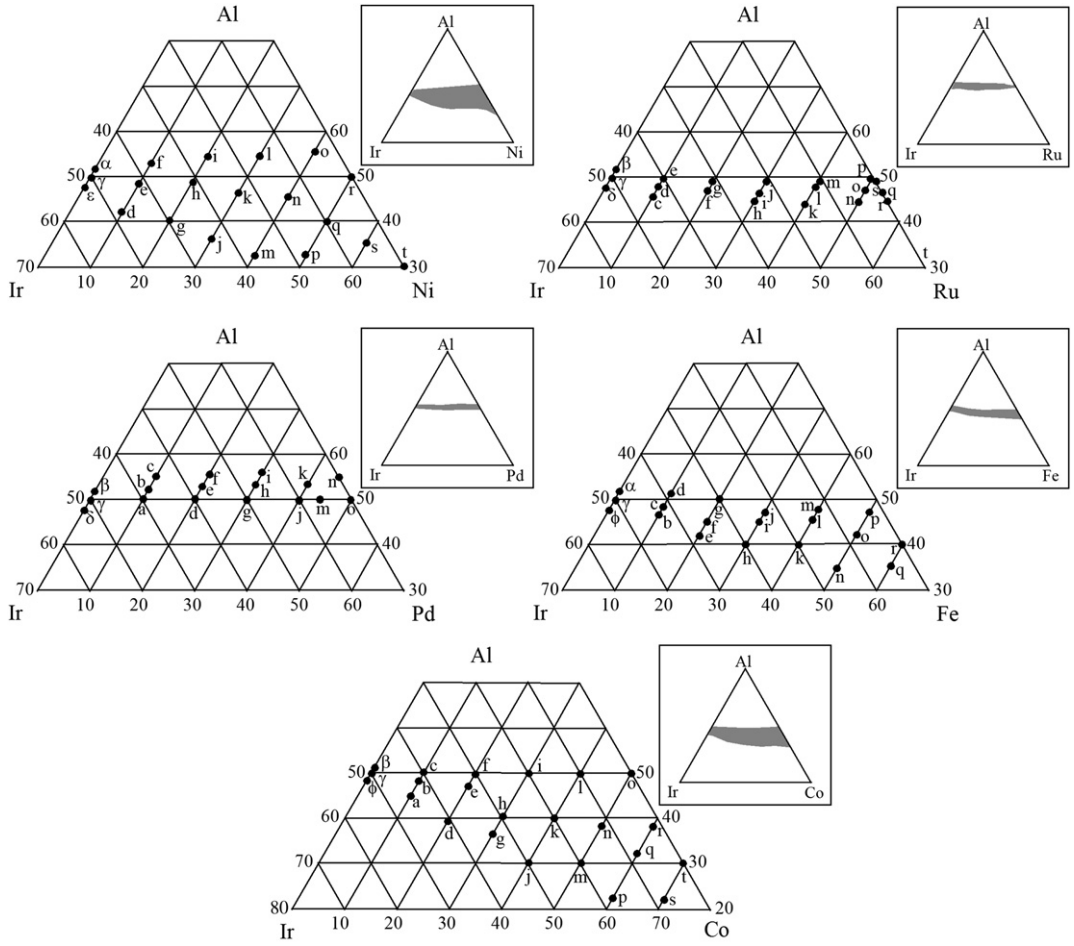

Fig. 1. Location of the alloys studied in this work in the ternary Al–Ir–X (X = Ni, Ru, Pd, Co, Fe) phase diagrams. The insets sketch, for each case, the full extent of the B2 field (observed experimentally). All concentrations are denoted in at%.

of the actual crystallographic structure of these phases. BANN simulations, due to its more accurate treatment of diffusion, provides a better comparison of the annealing process with experiment. It was found that, as expected, all the alloys studied in this work evolve to a B2 phase with substitutional distribution of the ternary additions in available lattice sites in each sublattice of the Al–Ir matrix. In each one of the ternary systems considered here, the B2 field was determined from known ternary phase diagrams Al–Ir–X (X = Ni, Ru, Pd, Co, Fe) and from simulations obtained in this work. With minor variations from one case to another, they all exhibit a continuous B2 field limited by AlIr and AlX. A sketch showing the location of the B2 field in each case is shown in Fig. 1, in addition to a detailed location of the many alloys studied in this work. A list of these alloys and their precise concentrations is displayed in Table 3. In the case of Ru, this entails a very narrow field of concentrations, which is somewhat wider for all the other elements. For Pd, the phase diagram exhibits ample solubility at each end of the field but with doubtful continuity between them for intermediate Pd concentrations. In spite of this anomaly, the results presented below consider it as a continuous field.

To reproduce the main features of the phase diagrams, BANN and MCAS simulations were performed for selected concentrations (listed in Table 3) within the limits of the known B2 field. In every single case, BANN simulations predicted a B2 phase, as expected, but with indications of a more complex low temperature phase structure.

Al–Ir–Ni: the high solubility between Ni and Ir results in very clearly defined B2 Al(Ir,Ni) alloys for all concentrations, with Ni occupying available sites without the creation of antistructure defects. It is only in MCAS simulations, which assume unrestricted diffusion, that a mild trend towards the formation of a Ni_3Al precipitate at low temperatures is observed.

Al–Ir–Pd: while BANN simulations once again predict the formation of a B2 phase, MCAS simulations suggest an AlIr–AlPd split at low temperatures, consistent with the experimental phase diagram.

Al–Ir–Fe: as with all the other ternary additions, BANN simulations predict the formation of a B2 ternary phase. However, there are some features worth noting. Fe exhibits a strong preference for Ir sites, creating a noticeable amount of antisite defects. As the concentration of Ir decreases, this ultimately leads (in MCAS simulations) to the formation of a Fe precipitate with Al in solution, Fe(Al), making AlIr + Fe(Al) the most common low temperature phase structure in most cases. Conversely, as the Al concentration grows, Fe(Al) turns into an ordered Fe_3Al phase and, for high Al concentrations, equiatomic FeAl. This transition from Fe(Al) to FeAl is observed regardless of the amount of Ir. Moreover, in those cases with enough excess Al, the Fe-rich phase splits into Fe_3Al and FeAl.

Al–Ir–Co: not surprisingly, Co follows the general pattern observed for Fe. BANN simulations, which predict a B2 ternary phase for all the alloys considered, clearly highlight the strong preference of Co for Ir sites. As in the case of Fe, MCAS simulations

Table 3
Labels (L) of the Al–Ir–X (X = Ni, Ru, Pd, Co, Fe) alloys studied in this work (concentrations in at%).

Ni	Al	Ir	L	Ru	Al	Ir	L	Co	Al	Ir	L	Fe	Al	Ir	L	Pd	Al	Ir	L
0	52	48	α	0	51	49	β	0	51	49	β	0	52	48	α	0	51	49	β
10	54	36	*f*	10	47	43	*d*	10	51	39	*c*	10	51	39	*d*	10	50	40	*a*
20	55	25	*i*	30	47	23	*i*	20	50	30	*f*	20	50	30	*g*	20	50	30	*d*
30	56	14	*l*	40	48	12	*l*	30	50	20	*i*	30	48	22	*j*	30	50	20	*g*
40			o	50	47	3	*o*	40	50	10	*l*	40	48	12	*m*	45	50	5	*m*
				52	48	0	*r*	50	50	0	*o*	50	48	2	*p*	50	50	0	*o*
0	50	50	γ	0	50	50	γ	0	50	50	γ	0	50	50	γ	0	50	50	γ
10	48	42	*e*	10	48	42	*e*	10	47	43	*b*	10	48	42	*c*	10	53	37	b
20	47	33	*h*	20	48	32	*g*	20	46	34	*e*	20	45	35	*f*	20	53	27	e
30	46	24	*k*	30	48	22	*j*	30	40	30	*h*	30	45	25	*i*	30	53	17	h
40	45	15	*n*	40	50	10	*m*	40	40	20	*k*	40	45	15	*l*	40	53	7	k
60	35	5	*r*	50	49	1	*p*	50	38	12	*n*	50	42	8	*o*	45	45	10	l
				51	49	0	*s*	60	35	5	*q*	60	40	0	*r*				
0	48	52	ε	0	49	51	δ	0	47	53	φ	0	47	53	φ	0	49	51	δ
10	42	48	*d*	10	45	45	*c*	10	43	47	*a*	10	46	44	*b*	10	54	36	*c*
20	40	40	*g*	20	47	33	*f*	20	38	42	*d*	20	42	38	*e*	20	55	25	*f*
30	35	35	*j*	30	46	24	*h*	30	35	35	*g*	30	40	30	*h*	30	55	15	*i*
40	33	27	*m*	40	45	15	*k*	40	32	28	*j*	40	40	20	*k*	40	50	10	*j*
50	33	17	*p*	50	46	4	*n*	50	30	20	*m*	50	35	15	*n*	45	55	0	*n*
50	50	0	*s*	53	47	0	*q*	60	25	15	*p*	60	34	6	*q*				
								70	25	5	*s*								

The greek letters label the binary Al–Ir alloys. The alloys are grouped, for each element, in order to match the graphical description in Fig. 1.

hint to the formation of a Co precipitate with Al in solution for high Co concentration, Co(Al). The dominant behavior is the formation of an AlIr matrix, so Co(Al) turns into Co_3Al as more Al becomes available after the formation of AlIr. Unlike the case of Fe, where ultimately this leads to the formation of AlFe or the coexistence of AlFe and Fe_3Al, there is mild evidence for the formation of AlCo or a Co_3Al/CoAl split.

Al–Ir–Ru: BANN shows the presence of a B2 ternary phase for all the concentrations studied. Ru shows no strong preference for either sublattice, but tends to occupy Ir sites. MCAS simulations, while conserving the B2 phase, show indication of Ru_3Al and RuAl formation at very low temperatures following the same patterns seen in the other cases, where the transition from Ru(Al) to $Ru_3Al + RuAl$ takes place as the concentration of Al increases.

In general, then, all BANN simulations reproduce the known features of the phase diagram for all ternary additions. MCAS simulations, which give information on the idealized ground state (where unrestricted diffusion allows for the formation of very low temperature second phases), show hints of X-rich phases with different degrees of order, depending on the concentration of Al: an X(Al) solid solution for low Al content, to a B2 AlX precipitate or, as in the Fe or Ru cases, $X_3Al + XAl$, for high Al content.

Site preference patterns were investigated for all cases, following the guidelines of previous applications of BFS, where details of the calculations can be found [23]. Computational cells were built with two competing types of defects: a 'direct' substitution where the addition X occupies an available site, X(Al) in an Ir-rich alloy or X(Ir) in the Al-rich case, or an 'indirect' substitution where the addition goes to the sublattice with the majority element creating an antistructure defect by displacing the atom to the available lattice site in the other sublattice (X(Ir)Al in the Ir-rich alloy or X(Al)Ir in the Al-rich case).

It was found that all ternary additions (Ni, Ru, Pd, Co, Fe) favor direct substitutions X(Ir) in Al-rich alloys, highlighting the fact that this creates Al–X bonds wich are, in all cases, energetically favorable. The other option (X(Al)Ir) is unfavorable due to the high energy cost of creating an Al(Ir) antisite defect and the increase in energy due to the many X–Ir bonds created.

In the case of Ir-rich alloys, Ni and Ru also favor direct substitutions in available Al sites, X(Al), while Pd, Co and Fe favor indirect substitutions, occupying Ir sites and displacing the Ir atom to the available site in the Al sublattice, X(Ir)Al. This varied behavior among the different additions is the result of a subtle balance of energy gains and losses. A direct substitution, X(Al), implies the formation of X–Ir bonds which is, in all cases, energetically less favorable than X–Al bonds. The indirect substitution, X(Ir)Al, implies the formation of an antisite defect, Ir(Al), when the Ir atom is displaced by the incoming X atom. There is a high energy cost in the formation of the antistructure Ir(Al) defect but it is somehow offset by the X–Al bonds thus created. This is a situation that perfectly describes the behavior of Pd due to the large gains when creating Pd–Al bonds, which largely outweigh the energy cost of forming an antistructure Ir(Al) atom. The case of Co and Fe is similar, but the balance (loss in forming Ir(Al), gain in forming X–Al bonds) is much closer, with a slight net benefit. For the case of X = Ni or Ru, a different picture emerges. Substitutions in Al sites create X–Ir bonds which are (for all five elements) less favorable. However, the energy cost in creating Ni–Ir or Ru–Ir bonds is not as large as in the other cases, making direct X(Al) substitutions likely. Indirect substitutions, as in the other cases, suffer from the formation of Ir(Al) antisite defects but are offset by the gain in forming X–Al bonds. In the case of Ni and Ru, the low energy cost of forming Ni–Ir or Ru–Ir bonds is such that direct substitutions exhibit a net advantage. It should be noted, however, that the net gain is exceedingly small and that relaxation effects or changes in local concentration could alter the balance making X(Ir)Al substitutions just as likely.

Details regarding short and long range order in these alloys were also computed for all the systems in this work. All five ternary systems Al–Ir–X share a basic feature, namely, the energetically favorable formation of Al–X bonds and less favorable Ir–X bonds. This has an impact on the level of ordering achieved in each case, as all additions X will compete with Ir in forming bonds with Al but will do so depending on the obstacle imposed by the ensuing formation of Ir–X bonds which, in general, will lead to less short and long range order as the concentration of X increases. In addition, temperature will have its own impact on the resulting degree of order. One way to quantify the degree of order is by examining the probabilities a_{AB} and a_{AC} for an atom of species A to have a nearest-neighbor (NN) of species B or C, in a ternary A–B–C

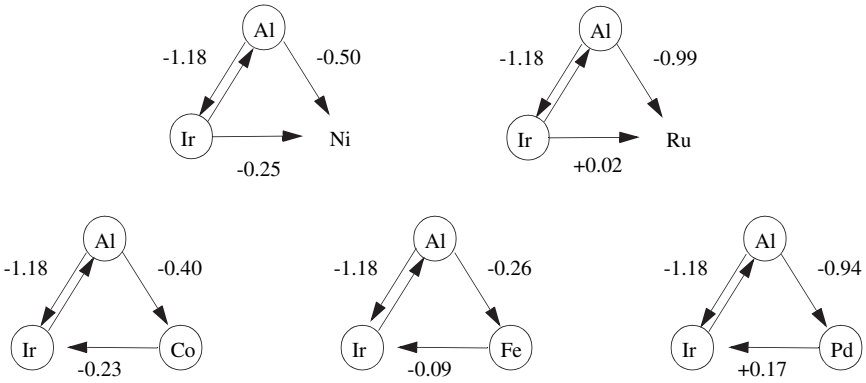

Fig. 2. Scheme representing the interaction between atoms of different species in a ternary alloy. The outgoing arrow from a circled atom indicates that the BFS contribution to the total energy of formation of the binary system formed by the two species at each end of the arrow is negative. The average bond energies (in eV/atom) in the binary cases (B2) are also shown.

system. The corresponding probabilities, b_{AB} and b_{AC}, for having B or C next-nearest-neighbors (NNN) give an indication of the long range degree of order.

Al–Ir–Ni: the NN probabilities a_{AlIr} and a_{AlNi} (probabilities that an Al atom has an Ir or a Ni atom, respectively, as a NN) and the corresponding NNN probabilities b_{AlIr} and b_{AlNi} are nearly constant up to $T = 1000$ K for systems with low Ni concentration. However, as the Ni concentration increases, the NN probabilities a_{AlIr} and a_{AlNi} show more noticeable changes with increasing temperature, ranging from nearly no change in a_{AlIr} for $x_{Ni} = 10$ at% to up to a 50% increase in a_{AlIr} for $x_{Ni} = 50$ at%, indicating that the effect of temperature favors the formation of Al–Ir over Al–Ni bonds. These results show some minor variation within the ternary B2 field, being more pronounced in alloys with high Al concentration than those with a smaller Al:Ir ratio. The NNN probabilities, b_{AlIr} and b_{AlNi} exhibit the same behavior in terms of dependence on temperature or location in the B2 field, but the overall trends with respect to a_{AlIr} and a_{AlNi} are reversed: b_{AlIr} decreases with temperature while b_{AlNi} increases, which is consistent with the prevalence of Al–Ir B2 ordering over Al–Ni.

Al–Ir–Ru: the coordination probabilities show remarkable stability with temperature and Ru concentration, which is likely to be the result of the strong Al–Ni and Al–Ru bonds. Unlike the Al–Ir–Ni system, there is no noticeable change other than the expected disorder near the melting temperature.

Al–Ir–Pd: similar to Al–Ir–Ru, and likely due to the same reasons (the high stability of the AlIr and AlPd phases) this system shows hardly any change in the coordination probabilities for all Pd concentrations and temperature. Disorder sets in rather sharply near the melting temperature.

Al–Ir–Co: this system shows some features that resemble those of the previously discussed Al–Ir–Ni system in terms of the quantitative changes in the coordination probabilities, which show a slightly stronger dependence with temperature and Co concentration, indicating a very unstable ordering. This is somewhat counterintuitive, given the stronger Al–Co bonding relative to Al–Ni. The Al–Ir–Co system evolves towards greater values of a_{AlCo} with increasing temperature but it is still highly sensitive to disorder with increasing Co concentration.

Al–Ir–Fe: of all the ternary systems studied, Al–Ir–Fe shows signs of long range order instability even at low temperatures ($T > 400$ K) for all the Fe concentrations studied. The short range a_{AlIr} and a_{AlFe} coordination probabilities are however rather stable indicating that in spite of the drastic difference in Al–Ir and Al–Fe bonding, neither element is strictly favored.

To understand the similarities and differences between the different ternary systems, it is useful to exploit a feature of the BFS method that gives information that supplements that provided by the coordination probabilities, resulting on a convenient way to understand the observed features. In the BFS context, each atom in the alloy contributes to the total energy of the system. When forming an alloy, if the total energy contribution of a given atom of species A is negative, it means that it lowers the energy of formation of the alloy thus facilitating the alloying process. Conversely, atoms with positive total energy contributions can be understood as atoms inhibiting the formation of the alloy. Fig. 2 shows a simple scheme that represents the interaction between Al, Ir and Ni atoms in a ternary Al–Ir–Ni alloy. The Al atom has two outgoing arrows, representing the fact that Al is the 'alloying species' (i.e., lowers the energy of formation) both when interacting with Ir and also with Ni. Similarly, the outgoing arrows in Ir indicate that Ir also contributes negatively to the energy of formation of AlIr and IrNi alloys (the latter form a continuous solid solution for the whole concentration range). The numbers labeling each of the 'bonds' between the atoms is the value of the energy of formation per atom in each of the binary combinations noted.

The behavior discussed above for the ordering trends in Al–Ir–Ni can then be described within the framework of this simple scheme. Both Ir and Al 'attract' Ni atoms (in the sense that Al is the alloying species, as discussed above, lowering the energy of formation in the presence of Ni), but the Al–Ni bonding far outweighs Ir–Ni. With Al–Ir being the stronger component of this scheme, it is then easy to understand the behavior of the coordination probabilities, which highlight the strong Al–Ir bonding over Al–Ni, and more so with increasing Ni concentration when the energy gains would otherwise be diminished if Al–Ni bonding was preferred. The case of Ru corresponds to a similar scheme, where both Ir al Al 'attract' Ru. The main difference with the Al–Ir–Ni scheme resides in the values of the average bond energies. In this case, Al–Ru bonds are in direct competition with Al–Ir bonds, and the energy gains provided by Ir when bonding with Ru become irrelevant due to their net positive contribution to the total energy of formation. It is then clear why this system (and its ordering behavior) is less sensitive than Al–Ir–Ni, with nearly constant values of the coordination probabilities up to the melting temperature.

The other three elements can be described by similar schemes, where Al 'attracts' the third atom (Co, Pd, or Fe) and the third atom 'attracts' Ir. The only difference resides in the relative values of their average bond energies. In the Co case, Ir is 'attracted' both by Al and Co. However, Al–Co bonding is nearly twice as strong as Ir–Co, resulting in a net gain for Al–Co. The energy gains are relatively small anyway, making the stability of the ordering scheme more susceptible to change with increasing temperature. This pattern repeats itself in the Fe case, only that very low energy gains (as

Table 4a
Energy of formation (ΔH), bulk modulus (B_0), zero-temperature equilibrium lattice parameter (a), average coefficient of thermal expansion (α), specific heat (C_v) and melting temperature (T_m) for the selected Al–Ir–Ni alloys.

L	Al (at%)	Ir (at%)	Ni (at%)	ΔH (eV/at)	B_0 (GPa)	a ($T=0$ K) (Å)	α (10^{-6} K^{-1})	C_v (10^{-4} eV/K)	T_m (K)
ε	48	52	0	−1.060	229.88	3.0434	9.81	1.08	2656
γ	50	50	0	−1.125	227.63	3.0370	9.92	1.09	2645
α	52	48	0	−1.065	220.37	3.0409	10.20	1.09	2586
d	42	48	10	−0.987	231.32	3.0240	9.88	1.06	2640
e	48	42	10	−1.025	217.24	3.0192	10.00	1.08	2546
f	54	36	10	−0.855	195.45	3.0311	11.38	1.08	2373
g	40	40	20	−0.877	220.48	3.0056	10.42	1.05	2537
h	47	33	20	−0.894	203.03	3.0009	11.20	1.07	2417
i	55	25	20	−0.671	173.81	3.0162	12.69	1.07	2188
j	35	35	30	−0.747	216.80	2.9886	10.70	1.03	2480
k	46	24	30	−0.788	189.38	2.9767	12.04	1.07	2298
l	56	14	30	−0.499	152.02	2.9954	14.31	1.07	2007
m	33	27	40	−0.643	206.23	2.9648	11.34	1.03	2380
n	45	15	40	−0.683	175.20	2.9461	13.05	1.08	2179
p	33	17	50	−0.575	191.32	2.9302	12.31	1.04	2257
r	35	5	60	−0.501	169.62	2.8803	13.90	1.07	2096
s	50	0	50	−0.581	143.29	2.8896	12.31	0.88	1953

compared to the Al–Ir–Co case) make the ordering scheme more sensitive to changes in temperature and concentration than the previous cases. Finally, while the Al–Ir–Pd system shows features similar to the other schemes, the energy balance is drastically different. In this case, Al–Pd bonding is in direct competition with Al–Ir bonding, and there is little interference from the unfavorable contributions from Ir–Pd, thus leading to a very stable ordering pattern with respect to changes in temperature or Pd concentration.

Based on the results of BANN simulations, the dependence of the thermal and physical properties of each alloy were computed, summarized in Table 4. The extensive amount of data that can be obtained clearly exceeds what can be sensibly presented here, so the display of results is limited to the room temperature values for the cohesive energy, equilibrium lattice parameter and bulk modulus. The coefficient of thermal expansion (CTE) is computed using an algorithm which has proven to be effective for multicomponent systems, described in detail in Ref. [19]. It should be noted that when comparing the predicted values of the CTE with experimental values, it is necessary to keep in mind that experimental measurements are based on changes in thermal dilation, whereas the computed values result from relative changes in the lattice parameter. These two quantities agree exactly only in the absence of structural vacancies [24]. The present calculations do not include structural vacancies thus resulting on estimates of the CTE that are bound to have noticeable differences with the experimental values. In the absence of reliable information on the defect structure of the alloys considered in this work, the values in Table 4 do not include structural vacancies. It is however likely that the resulting trends and changes in the predicted values of the CTE with temperature and concentration of the ternary element will not differ much from those that could be eventually be measured experimentally.

As mentioned above, we simplify the presentation of results by limiting it to the zero temperature and room temperature values of the lattice parameter, and the average value of the CTE between 300 and 1200 K, from which all the necessary intermediate data can be derived.

For the calculation of the heat capacity, C_v, we use the expression [25]

$$C_v = \frac{\alpha B_0 V}{\gamma} \tag{2a}$$

where α is the CTE, B_0 is the bulk modulus, V is the atomic volume and γ is Gruneisen's constant. Using the expressions for γ and B_0 in

Table 4b
Energy of formation (ΔH), bulk modulus (B_0), zero-temperature equilibrium lattice parameter (a), average coefficient of thermal expansion (α), specific heat (C_v) and melting temperature (T_m) for the selected Al–Ir–Ru alloys.

L	Al (at%)	Ir (at%)	Ru (at%)	ΔH (eV/at)	B_0 (GPa)	a ($T=0$ K) (Å)	α (10^{-6} K^{-1})	C_v (10^{-4} eV/K)	T_m (K)
δ	49	51	0	−1.110	229.46	3.0388	9.84	1.08	2657
γ	50	50	0	−1.125	227.63	3.0370	9.92	1.09	2645
β	51	49	0	−1.134	225.54	3.0356	10.01	1.09	2631
c	45	45	10	−1.043	235.55	3.0372	9.74	1.07	2643
d	47	43	10	−1.068	231.61	3.0344	9.90	1.08	2617
e	48	42	10	−1.094	229.95	3.0320	9.97	1.09	2609
f	47	33	20	−1.039	229.15	3.0285	10.13	1.09	2546
g	48	32	20	−1.041	226.77	3.0279	10.23	1.09	2529
h	46	24	30	−0.977	227.92	3.0255	10.31	1.08	2480
i	47	23	30	−1.000	226.38	3.0233	10.39	1.09	2471
j	48	22	30	−1.018	224.40	3.0213	10.48	1.09	2460
k	45	15	40	−0.934	227.50	3.0209	10.47	1.08	2421
l	48	12	40	−0.983	222.13	3.0155	10.73	1.10	2386
m	50	10	40	−0.965	216.14	3.0157	10.92	1.09	2343
n	46	4	50	−0.921	223.50	3.0130	10.81	1.09	2338
o	47	3	50	−0.937	221.73	3.0111	10.90	1.10	2326
p	49	1	50	−0.950	217.03	3.0088	11.13	1.10	2295
q	47	0	53	−0.928	221.07	3.0092	10.98	1.10	2305
r	48	0	52	−0.943	219.07	3.0083	11.07	1.10	2299
s	49	0	51	−0.965	217.58	3.0068	11.13	1.11	2295

Table 4c
Energy of formation (ΔH), bulk modulus (B_0), zero-temperature equilibrium lattice parameter (a), average coefficient of thermal expansion (α), specific heat (C_v) and melting temperature (T_m) for the selected Al–Ir–Pd alloys.

L	Al (at%)	Ir (at%)	Pd (at%)	ΔH (eV/at)	B_0(GPa)	a ($T=0$ K) (Å)	α (10^{-6} K^{-1})	C_v (10^{-4} eV/K)	T_m (K)
β	51	49	0	−1.134	225.54	3.0356	10.01	1.09	2631
γ	50	50	0	−1.125	227.63	3.0370	9.92	1.09	2645
δ	49	51	0	−1.110	229.46	3.0388	9.84	1.08	2657
a	50	40	10	−1.027	210.55	3.0462	10.74	1.09	2450
b	53	37	10	−0.943	199.72	3.0523	11.22	1.09	2364
c	54	36	10	−0.901	195.63	3.0559	11.41	1.09	2330
d	50	30	20	−0.948	194.08	3.0550	11.67	1.09	2262
e	53	27	20	−0.855	182.90	3.0630	12.26	1.09	2173
f	55	25	20	−0.773	174.85	3.0710	12.71	1.08	2105
g	50	20	30	−0.901	178.92	3.0623	12.71	1.09	2087
h	53	17	30	−0.793	167.18	3.0729	13.44	1.09	1991
i	55	15	30	−0.723	159.62	3.0807	13.95	1.09	1928
j	50	10	40	−0.902	165.50	3.0660	13.83	1.10	1930
k	53	7	40	−0.766	152.77	3.0808	14.76	1.09	1823
l	45	10	45	−0.842	168.92	3.0726	13.68	1.08	1918
m	50	5	45	−0.860	157.15	3.0730	15.22	1.15	1834
n	55	0	45	−0.719	139.24	3.0906	16.12	1.09	1691
o	50	0	50	−0.883	151.40	3.0722	14.58	1.06	1765

Table 4d
Energy of formation (ΔH), bulk modulus (B_0), zero-temperature equilibrium lattice parameter (a), average coefficient of thermal expansion (α), specific heat (C_v) and melting temperature (T_m) for the selected Al–Ir–Co alloys.

L	Al (at%)	Ir (at%)	Co (at%)	ΔH (eV/at)	B_0(GPa)	a ($T=0$ K) (Å)	α (10^{-6} K^{-1})	C_v (10^{-4} eV/K)	T_m (K)
β	51	49	0	−1.134	225.54	3.0356	10.01	1.09	2631
γ	50	50	0	−1.125	227.63	3.0370	9.92	1.09	2645
ϕ	47	53	0	−1.049	232.11	3.0449	9.72	1.07	2670
a	43	47	10	−0.817	224.19	3.0348	10.20	1.05	2544
b	47	43	10	−0.901	217.40	3.0265	10.50	1.07	2504
c	51	39	10	−0.901	207.33	3.0237	10.96	1.08	2432
d	38	42	20	−0.614	220.22	3.0216	10.56	1.04	2447
e	46	34	20	−0.762	205.69	3.0048	11.28	1.07	2360
f	50	30	20	−0.824	197.88	2.9955	11.70	1.09	2312
g	35	35	30	−0.474	213.84	3.0004	11.09	1.03	2339
h	40	30	30	−0.549	204.03	2.9907	11.61	1.05	2278
i	50	20	30	−0.671	183.02	2.9676	12.88	1.10	2145
j	32	28	40	−0.387	210.42	2.9712	11.58	1.03	2251
k	40	20	40	−0.485	193.61	2.9529	12.57	1.07	2145
l	50	10	40	−0.578	170.48	2.9252	14.21	1.13	2000
m	30	20	50	−0.309	205.19	2.9362	12.24	1.04	2149
n	38	12	50	−0.421	188.60	2.9108	13.36	1.09	2047
o	50	0	50	−0.508	159.20	2.8672	15.82	1.19	1865

Table 4e
Energy of formation (ΔH), bulk modulus (B_0), zero-temperature equilibrium lattice parameter (a), average coefficient of thermal expansion (α), specific heat (C_v) and melting temperature (T_m) for the selected Al–Ir–Fe alloys.

L	Al (at%)	Ir (at%)	Fe (at%)	ΔH (eV/at)	B_0 (GPa)	a ($T=0$ K) (Å)	α (10^{-6} K^{-1})	C_v (10^{-4} eV/K)	T_m (K)
ϕ	47	53	0	−1.049	232.11	3.0449	9.72	1.07	2670
γ	50	50	0	−1.125	227.63	3.0370	9.92	1.09	2645
α	52	48	0	−1.065	220.37	3.0409	10.19	1.09	2586
b	46	44	10	−0.865	218.78	3.0301	10.51	1.07	2488
c	48	42	10	−0.901	215.05	3.0263	10.69	1.08	2465
d	51	39	10	−0.885	206.96	3.0257	11.06	1.09	2406
e	42	38	20	−0.644	211.85	3.0168	11.12	1.07	2346
f	45	35	20	−0.681	205.61	3.0130	11.44	1.08	2306
g	50	30	20	−0.717	194.35	3.0070	12.06	1.10	2229
h	40	30	30	−0.480	202.63	2.9959	11.97	1.08	2189
i	45	25	30	−0.536	192.08	2.9879	12.62	1.10	2120
j	48	22	30	−0.533	184.08	2.9863	13.12	1.11	2065
k	40	20	40	−0.369	191.50	2.9637	13.08	1.10	2017
l	45	15	40	−0.390	179.01	2.9571	14.07	1.13	1935
m	48	12	40	−0.400	171.70	2.9532	14.65	1.14	1885
n	35	15	50	−0.253	194.13	2.9320	13.62	1.11	1933
o	42	8	50	−0.285	177.02	2.9186	15.00	1.16	1819
p	48	2	50	−0.267	159.96	2.9110	16.60	1.20	1704
q	34	6	60	−0.212	191.57	2.8821	14.69	1.16	1806
r	40	0	60	−0.229	176.46	2.8664	16.13	1.21	1704

Ref. [26] and the CTE computed using the methodology described in Ref. [19], the heat capacity is then

$$C_v = \frac{E_c \bar{\alpha} V}{4.56\pi r_{ws}^2 l} \tag{2b}$$

where $\bar{\alpha}$ is the averaged CTE, E_c is the cohesive energy, r_{ws} is the Wigner–Seitz radius (which can derived from the value of the lattice parameter listed in Table 4) and l is the scaling length for the alloy.

Again, being that they mostly follow the behavior of the CTE, only the room temperature value is listed. Finally, the melting temperature, T_m, is determined from the known concept that the inflexion point in the binding energy of the alloy is a measure of the thermal energy necessary for melting, as described in Ref. [26],

$$T_m = \frac{0.032 E_c}{k_B} \tag{3}$$

where E_c is the cohesive energy and k_B is Boltzmann's constant.

Although all the alloys in this work are Al–Ir based, as a way to validate the predictions for the melting temperature of the ternary systems, it is interesting to note the methodology gives good estimates for the melting temperature of the basic B2 Al–X systems. The most accurate predictions (2% error) correspond to AlNi, AlRu, and AlCo, with $T_m = 1911$ K [27], 2333 K [28], and 1913 K [29], respectively. Slightly larger deviation (4%) is found for AlFe ($T_m = 1583$ K [29]). The largest deviation is found for AlIr (10%), where the experimental value is $T_m = 2393$ K [30]. It should be noted that, beyond the limitations due to the simplicity of the model from which the theoretical results were obtained (see Eq. (3)) and the fact that the cohesive energy is evaluated from numerical simulations, it is also possible that the presence of thermal vacancies could have an effect in the magnitude of T_m which is not included in the present calculation. In the particular case of AlIr, the base alloy in this study, this is an important factor that has to be taken into account. Estimates of the behavior of T_m in the narrow field of the B2 phase (which extends between 48 and 52 at% Ir) suggest that the melting temperature is maximum for the equiatomic case. The calculations, within their range of validity, neither confirm nor contradict this fact, as the changes (see Table 4) are very small and subject to change depending on minor changes in the outcome of the simulation.

While Table 4 provides all the relevant results, some additional insight can be obtained from a cursory review of the different properties, especially if grouped as in Table 3. However, this choice is arbitrary and different behavior can be extracted whether the results are examined as a function of Al, Ir, or X concentration. For example, in addition to the numerical results shown in Table 4 for the heat capacity, melting temperature, and CTE, Fig. 3 displays results for $Al_{50}Ir_{50-x}X_x$ ($x = 0$–50 at%) alloys. The melting temperature displays a clear linear behavior, with Ru showing a much slower decrease in T_m with increasing concentration. A rather linear behavior also describes the increase in CTE for all alloying additions, with Ru again trailing the others. While the changes in melting temperature and CTE can be as large as 60% (relative to AlIr), the changes in the heat capacity values are very small and hardly noticeable. The scatter in the C_v results is basically a consequence of the fluctuations in the values of the quantities that appear in the calculation of C_v. These fluctuations can be significant, given the wide range of change of these quantities, once they are combined in the calculation of C_v. The distinct behavior of Ru in Fig. 3, added to the much milder linear decrease of the bulk modulus for increasing X concentration and increasing Al:Ir ratio singles out Ru as a special case. In spite of minor differences between the different additives X, most display a monotonous behavior for the whole range of concentrations (for each group). However, a common feature appears in all the figures,

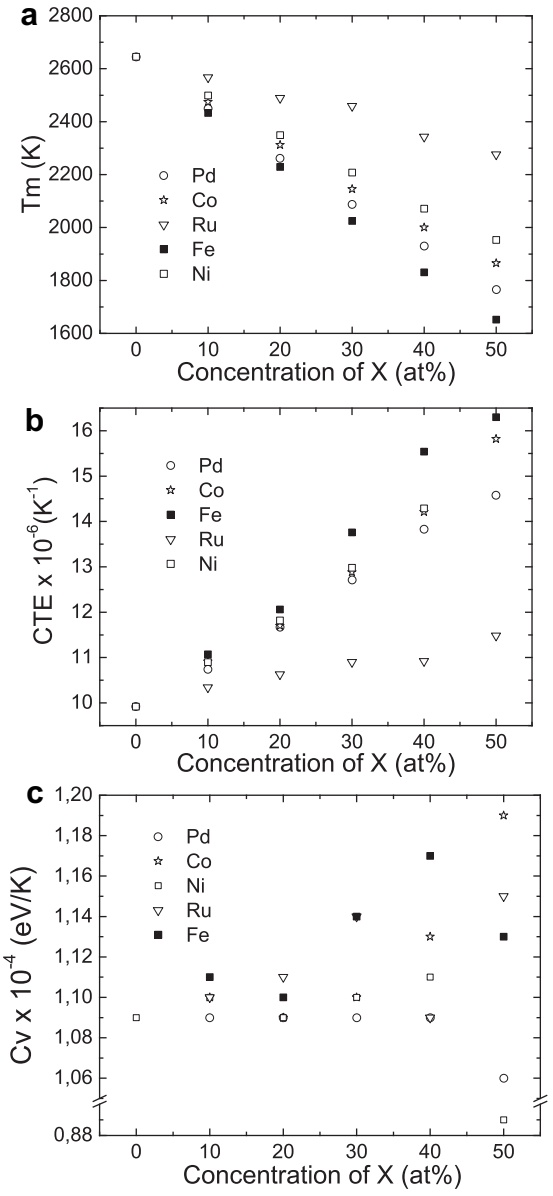

Fig. 3. (a) Melting temperature, (b) coefficient of thermal expansion, and (c) heat capacity for $Al_{50}Ir_{50-x}X_x$ ($x = 0$–50 at%) alloys.

namely, the rapid change (departing from the otherwise almost linear behavior) while approaching the high-X, low-Ir side of the phase diagram (right edge in Fig. 1), which corresponds to the AlRu, AlNi, AlFe, AlCo, AlPd binary cases. Keeping in mind that the groups defined in Table 3 are to some extent random (in the sense that there is no way to predetermine the 'path' along the B2 field that would correspond to a smooth change in properties), the plots hint to regular features that repeat themselves in every case. Most noticeable are the acceleration of the decrease in compressibility and the fact that there is a rebound in the value of the specific heat after reaching a minimum value as it approaches the binary Al–X case. Clearly related to this, there is also a change in the behavior of the coefficient of thermal expansion again close to the binary Al–X case. One other feature present in all cases is the substantial change from the upper region of the B2 field with high Al content (top groups in Table 3) to the bottom region, with the latter showing noticeable departures from the behavior that characterizes most of the B2 field. The nature of these changes, however, is not the same for different

elements X, in spite from the otherwise apparent similarities in the phase diagrams. The fact that these changes and differences exist, warrants future work to examine this properties in detail both experimentally and theoretically.

4. Conclusions

Atomistic modeling via quantum approximate methods allows for an economical but accurate description of properties of complex systems where experimental evidence is not abundant and technological applications require a detailed knowledge of their physical and thermal properties. In this work, we applied the BFS method for alloys and its extension to finite temperature to B2 Al–Ir–X (X = Ni, Ru, Pd, Co, Fe) alloys for the estimation of the phase structure within the recognized B2 field, site preference behavior, and analysis of short and long range ordering trends, and the variation with concentration of the lattice parameter, bulk modulus, cohesive energy, coefficient of thermal expansion, heat capacity and melting temperature.

Acknowledgements

Fruitful discussions with N. Bozzolo are gratefully acknowledged.

References

[1] Criscione JM, Mercuri RA, Schram EP, Smith AW, Volk HF. AFML-TDR-64-174, Part 2; January 1965.
[2] Evans UR. The corrosion and oxidation of metals. London: Edward Arnold Ltd; 1960. p. 13.
[3] Lee N, Worrell WL. Oxidation Metals 1989;32:357.
[4] Hosoda H, Miyazaki S, Hanada S. Intermetallics 2000;8:1081.
[5] Hosoda H, Wakashima K. Mater Sci Eng A 2003;352:16.
[6] Yamabe-Mitarai Y, Aoki H. Mater Sci Eng A 2003;362:152.
[7] Chiba A, Ono T, Li XG, Takahashi S. Intermetallics 1998;6:35.
[8] Yamabe-Mitarai Y, Aoyagi T, Nishida K, Auki H, Abe T, Murakami H. Intermetallics 2007;15:479.
[9] Hill PJ, Cornish LA, Witcomb MJ. J Alloy Compd 1998;280:240.
[10] Fleischer R, Field RD, Briant CL. Metall Trans A 1991;22:403.
[11] Hill PJ, Cornish LA, Witcomb MJ. J Alloy Compd 1999;291:130.
[12] Liu KW, Mücklich F. Intermetallics 2005;13:373.
[13] Vjunitsky I, Bandyopadhyay PP, Siegmann St, Dvorak M, Schönfeld E, Kaiser T, Steurer W, Shklover V. Surf Coat Technol 2005;192:131.
[14] Vjunitsky I, Schönfeld E, Kaiser T, Steurer W, Shklover V. Intermetallics 2005;13:35.
[15] Mosca HO, Bozzolo G, del Grosso MF. Mat Sci Eng B 2009;162:99.
[16] Katrych S, Weber Th, Kobas M, Massüger L, Palatinus L, Chapuis G, Steurer W. J Alloy Compd 2007;428:164.
[17] Pavlyuchkov D, Grushko B, Velikanova TY. J Alloy Compd 2008;453:191.
[18] Bozzolo G, Ferrante J, Smith JR. Phys. Rev. B 1992;45:493;
Bozzolo G, Garcés J, Noebe RD, Abel P, Mosca H. Prog Surf Sci 2003;73:79.
[19] Bozzolo G, del Grosso MF, Mosca HO. Mater Lett 2008;64:3975.
[20] Rose JH, Smith JR, Guinea F, Ferrante J. Phys Rev B 1984;29:2963.
[21] Blaha P, Schwartz K, Luitz J. WIEN97, Vienna University of Technology [Updated Unix version of the copyrighted WIEN code]. Blaha P, Schwartz K, Sorantin P, Trickey SB. Comput Phys Commun 1990;59:399.
[22] Gargano P, Mosca HO, Bozzolo G, Noebe RD. Scripta Mater 2003;48:695.
[23] Bozzolo G, Noebe RD, Mosca HO. J Alloy Compd 2005;389:80;
Bozzolo G, Mosca HO. Intermetallics 2007;254:392.
[24] Povolo F, Mosca HO. Phys Stat Sol A 1997;164:609.
[25] Raju S, Sivasubramanian K, Mohandas E. Mater Lett 2003;57:3793.
[26] Guinea F, Rose JH, Smith JR, Ferrante J. Appl Phys Lett 1984;44:53.
[27] Cao WB, Kirihara S, Miyamoto Y, Matsuura K, Kudoh M. Intermetallics 2002;10:879.
[28] Cao F, Nandy TK, Stobbe D, Pollock TM. Intermetallics 2007;15:34.
[29] Nakamura R, Takasawa K, Yamazaki Y, Iijima Y. Intermetallics 2002;10:195.
[30] Axler KM, Foltyn EM, Peterson DE, Hutchinson WB. J Less-Common Met 1989;156:213.